Journal of Structural Geology 112 (2018) 39–52

Contents lists available at ScienceDirect

Journal of Structural Geology

journal homepage: www.elsevier.com/locate/jsg

Role of grain-size in phyllonitisation: Insights from mineralogy, microstructures, strain analyses and numerical modeling

Narayan Bose, Dripta Dutta, Soumyajit Mukherjee*

Department of Earth Sciences, Indian Institute of Technology Bombay, Powai, Mumbai, 400 076, Maharashtra, India

ARTICLE INFO

Keywords:
Brittle shear
Microstructure
Rheology
Grain size
Fracture
Finite element modeling

ABSTRACT

Brittle Y- and P-planes exist in an exposure of greywacke in the Garhwal Lesser Himalaya, India. Although, Y-planes are well developed throughout, the P-planes are prominent only in some parts (domain-A), and not elsewhere (domain-B). To investigate why the P-planes developed selectively, the following studies were undertaken: *1.* Clay-separated XRD analyses: clinochlore and illite are present in both the domains. *2.* Strain analyses by R_f-φ method: it deduces strain magnitudes of ~1.8 for the ductile deformed quartz grains from both the domains A and B. *3.* Grain size analyses of quartz clasts: domain-A is mostly composed of finer grains (area up to 40,000 μm^2), whereas domain-B consists of a population of coarser grains (area > 45,000 μm^2). A 2D finite element modeling of linear elastic material was performed using COMSOL software to investigate the control of grain-size variation on the generation brittle shear planes. The results of numerical modeling corroborate the known fact that an increase in grain-size reduces the elastic strain energy density. A broader grain-size distribution increases the effects of diffusion creep and resists the onset of dislocation creep. Thus, rocks with coarser grain population (domain B) tend to resist the generation of shear fractures, unlike their fine-grained counterpart (domain A).

1. Introduction

Brittle shear tectonics has far-reaching implications in dynamic rupturing during earthquakes (Harris et al., 1991), in petroleum geosciences (Fjar et al., 2008) and in CO_2 sequestration (Cappa and Rutqvist, 2011). Brittle failure due to shear, which usually occurs at the upper crustal levels, produces several kinds of fractures, viz. Y, P, R etc. (Bartlett et al., 1981; Passchier and Trouw, 2005). Shear fractures preferably develop in the less competent zones (Treagus, 1988; Marinho and Gomes, 2013) undergoing higher strain (Kanagawa, 1993). Tang et al. (2000) reported that tensile fractures generated in a shear band leads to faulting. In nature, there may be insignificant movement along the shear fractures due to profound stress drop during fracturing (Mandl, 1999). Moreover, shearing produces hybrid fracture (Ramsey and Chester, 2004; Peacock et al., 2018), rather than a typical shear- or a tensile-fracture. Gudmundsson (2011) defines fractures and other brittle planes as mechanical discontinuities in the rock across which cohesion drops. Both shear- and normal-stress can be responsible for the failure. The author further asserts that, unlike the fracture surfaces, their tips do exhibit evidences of ductile deformation, and that fracture propagation does involve plasticity. Brittle shear zones may possess deformation markers, which are discontinuous across the shear fractures (Fossen and Cavalcante, 2017). Y- and P- planes are shear fractures (or shear joints), and are useful to decipher the shear sense (Passchier and Trouw, 2005; Peacock et al., 2016). The angle between Y- and P- plane can range from 10 to 45° (Meyer et al., 2017).

Experimental studies indicate that, as stress increases, material in general deforms elastically, till the elastic limit, followed by plastic deformation. During elastic deformation the strain energy is stored and can be used to regain the initial shape. On the other hand, in plastic deformation, the energy is consumed in the shape change (plastic elongation). Various lab experiments show that, under a constant strain rate, fine-grained rocks attain plasticity much earlier than the coarse-grained ones (e.g., Karato et al., 1986). Hence, plastic deformation is expected to be more ubiquitous in the former. Moreover, the yield stress tends to decrease with increase in grain size for n (stress exponent) > 2 (Twiss and Moores, 2007). For both dry and wet quartzites, n = 2.72 ± 0.19 (Koch et al., 1989). Quartz grains deformed under dislocation creep regime have n ~3 to 4 (Luan and Paterson, 1992; Gleason and Tullis, 1995; Rutter and Brodie, 2004). Morales et al. (2011) however, reported a wider range of n for quartzites: 1.4–5.7 with 2.75 as the mean value. Close to the brittle-ductile transition zone n = 5 (Fukuda and Shimizu, 2017 and references therein).

During brittle deformation grain-size reduces by brittle fracturing

* Corresponding author.
E-mail addresses: narayan.bghs@gmail.com (N. Bose), dripta.dutta@gmail.com (D. Dutta), soumyajitm@gmail.com (S. Mukherjee).

https://doi.org/10.1016/j.jsg.2018.03.010
Received 22 February 2018; Accepted 2 March 2018
Available online 18 April 2018
0191-8141/

(cataclasis; Passchier and Trouw, 2005). This may happen in several steps (Keulen et al., 2007) by recrystallization that perturbs the effect of stress on individual grains (TerHeege et al., 2002). This is true especially for quartz grains (Gueydan et al., 2005), where additionally secondary minerals precipitate during mylonite to ultramylonite transition (Kilian et al., 2011). However, the size of the recrystallised quartz grains is temperature-independent and remains unchanged after the nucleation process (Xia and Platt, 2018).

This work aims to check the effects of grain size in natural deformation. Y-planes are present throughout the studied rock exposure in the Lesser Himalaya, but P-fractures occur locally. From field observations, microstructural studies and numerical modeling, we investigate the mechanisms and controlling factors for the selective generation of P-planes. Mineralogical and microstructural studies were followed by strain- and grain size analyses. The results, thus obtained, were used in numerical modeling.

2. Geology

The study area is located at the Inner-Lesser Himalaya of the Uttarakhand district, India. The Proterozoic sedimentary rocks (greywacke/quartz arenite) present here belong to the Rautgara Formation (Fig. 1; Valdiya, 1980, 2010; Célérier et al., 2009; Dubey, 2014). These rocks have also been reported as the Netala Quartzite (Jain, 1971; Agarwal and Kumar, 1973). The grade of metamorphism is very low and it increases up to greenschist near the Main Central Thrust (MCT) zone towards N (e.g. Thakur, 1992; Metcalfe, 1993). The Munsiari Thrust, which is also the northern boundary of the Lesser Himalaya and the southern boundary of the MCT zone, is ~20 km E from the study location. The rocks have undergone two deformation phases (Agarwal and Kumar, 1973; Thakur and Kumar, 1994): *D1*- NE-SW compression that produced NW-SE trending folds (F_1; such as, Baragadi, Netala, Sialamgad Anticlines in Fig. 1) and axial planar faults (e.g. the Gangori-Jamak Fault), followed by *D2*- NW-SE compression that gave rise to ~ NE-SW trending folds (F_2). However, Pant et al. (2012) claimed that F_2 folds developed prior to F_1. The rare-earth-element studies and palaeo-current directions of the Rautgara Formation indicate its provenance in the Archean Aravalli-and Bundelkhand granitoids (Rashid, 2005; McKenzie et al., 2011).

3. Deformation structures and sample description

3.1. Outcrop-scale structures

The N-trending rock exposure (30°45.114′N, 78°27.189′E) is located ~ 3 km N of Uttarkashi along the Bhagirathi river section, Uttarakhand state, India. The near-vertical exposure of the rock is devoid of any meso-scale folding and ductile shear-sense indicators (Fig. 2a). Instead, it is brittle sheared, and we designate this as the "Gangori Shear Zone". Based on the presence of brittle Y- and P-planes, two domains were distinguished in the outcrop: 1. Domain A (Fig. 2a') - where both the Y- and the P- planes are present, 2. Domain B (Fig. 2b') - where only Y-plane is present and the P-plane is absent mesoscopically. The Y-planes in both these domains dip ~ SW. The shear sense deciphered from the P-planes is 'top-to-SW (down) extensional' i.e., normal fault like shear. Oriented samples were collected from domains-A and B.

3.2. Petrography of samples

The matrix content ranges 15–75% (by volume) and the framework is mostly quartz, along with few calcite (Fig. 3). Hence, as per Pettijohn's scheme (Pettijohn, 1984), rocks from domains A and B are greywacke. X-ray diffraction (XRD) analyses were performed on samples from domains A and B using the PANalytical Empyrean (PANalytical B.V., Almelo, The Netherlands) setup at IIT Bombay. The powdered (< 75 μm) samples were taken through decantation and centrifuge processes to separate the silts from clays. Then the air dried samples were studied followed by ethylene glycol (vapour) treatment. The reader can consult other articles (e.g., Moore and Reynolds, 1989; Poppe et al., 2001) for details of XRD studies. XRD results were analysed using the HighScore Plus software and the Inorganic Crystal Structure Database (ICSD). The samples from domains A and B consist

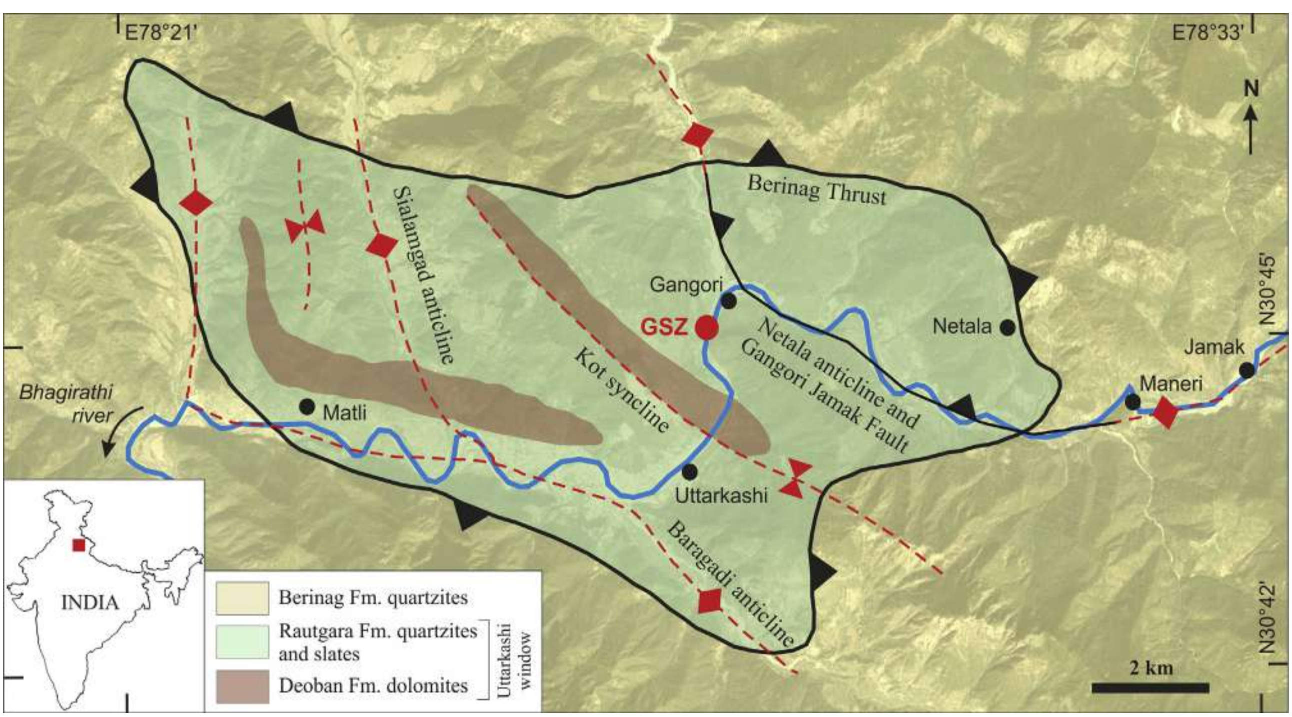

Fig. 1. Geological map compiled from Jain (1971), Agarwal and Kumar (1973), Valdiya (1980) and superposed on the Google Earth satellite imagery. Red filled square in the inset and the circle in the main figure indicate the study area: the Gangori Shear Zone (GSZ). Note near the location Maneri, unusual turn of the river is due to a dam constructed there. (For interpretation of the references to colour in this figure legend, the reader is referred to the Web version of this article.)

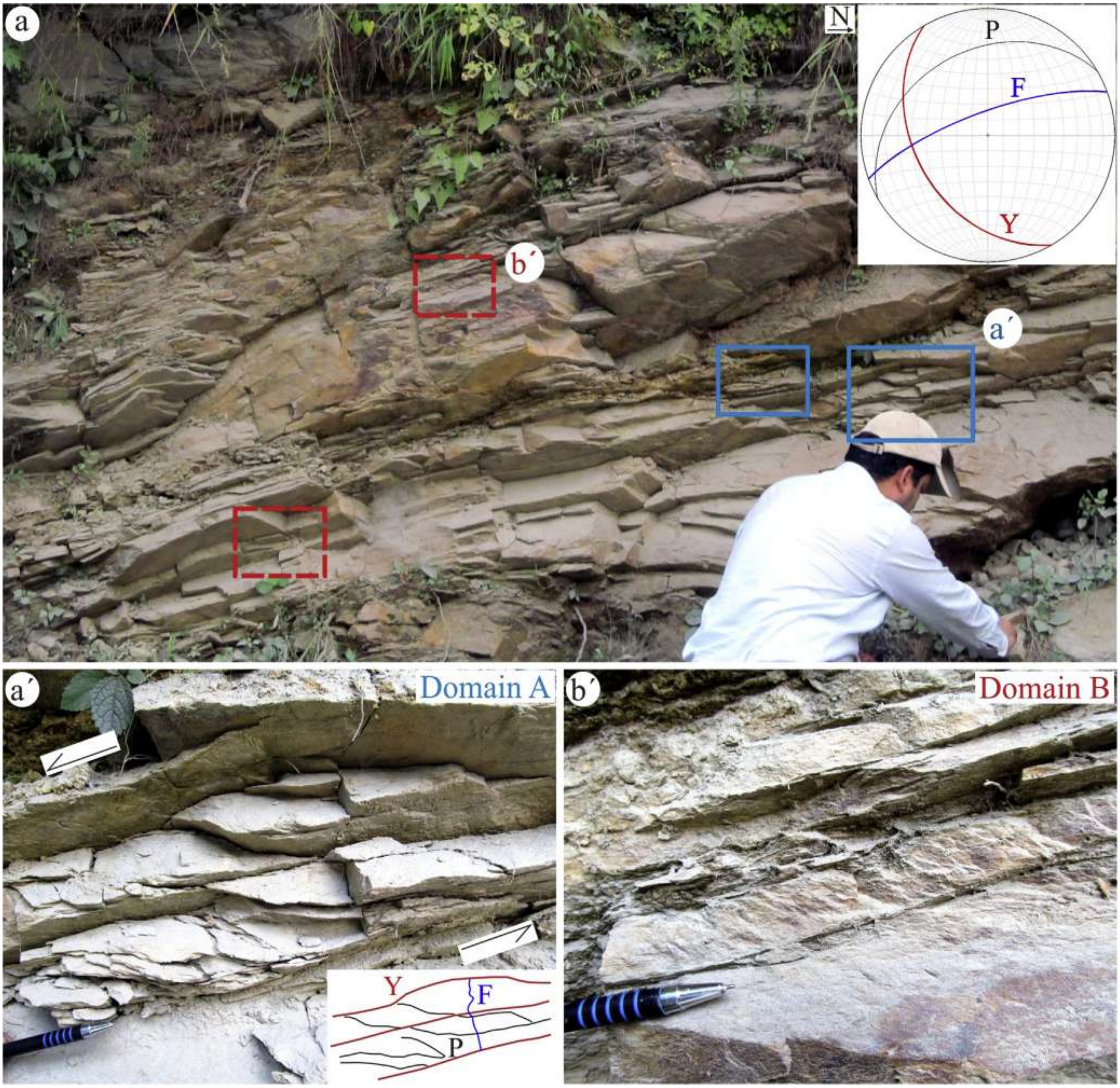

Fig. 2. Field observations. **(a)** Exposure at Gangori Shear Zone (GSZ). S. Mukherjee (~80 cm inside snap) as marker. Rectangles show the parts from where samples were collected. Blue solid rectangles: 'domain-A'; red-broken rectangles: 'domain-B'. Streoplot in the inset:Y-plane: 150°/42°→240°, P-plane: 60°/35°→330°, fracture plane: 70°/75°→340°. **(a′)** Domain-A: P-planes developed. ~6 cm of pen is visible, as marker. **(b′)** Domain-B: P-planes not developed. ~5 cm of pen is visible, as marker. (For interpretation of the references to colour in this figure legend, the reader is referred to the Web version of this article.)

of clinochlore and illite (Supplementary Fig. 1), which are common clay minerals in shear zones (e.g., Lacroix et al., 2012; Buatier et al., 2013). The glycolated study confirmed the absence of clays of expanding phases.

3.3. Microstructures

XZ-sections (perpendicular to the trend of Y-plane and parallel to the dip direction) of the oriented samples were used for microstructural investigation. Narrow range of grain size variations, curved shear planes, marginal recrystallization of quartz grains etc. indicate intense shearing in domain-A (Fig. 3a1, a2, a3). On the other hand, in domain-B coarser framework grains with symmetric- and asymmetric mantled porphyroclasts (Fig. 3b1, b2, b3) indicate broader grain-size distribution (quantification in Section-5). Although, the outcrop of domain-B is devoid of P-planes, evidences of intense ductile shear, deciphered from mantled porphyroclasts (Fig. 3b2, b3) and a few S-C fabrics (Fig. 3b1), were observed under an optical microscope. The micro-fractures present in the two domains are also dissimilar. The inter-granular extension fractures in domain A are mainly filled with clays and cross-cut the pre-existing ductily deformed veins and crenulations (Fig. 4). Whereas, in domain B, the less abundant inter-granular fractures are quartz-filled, with local drag along them (Fig. 5a, c). Moreover, grain-size reduction by intra-granular fracturing is more pronounced in domain B (Fig. 5a, b, d).

Domains A and B show various grain boundary mobility features (Stipp et al., 2002; Passchier and Trouw, 2005), such as: cataclastic flow (< 300 °C) is indicated by inter-granular fractures (Fig. 4) and

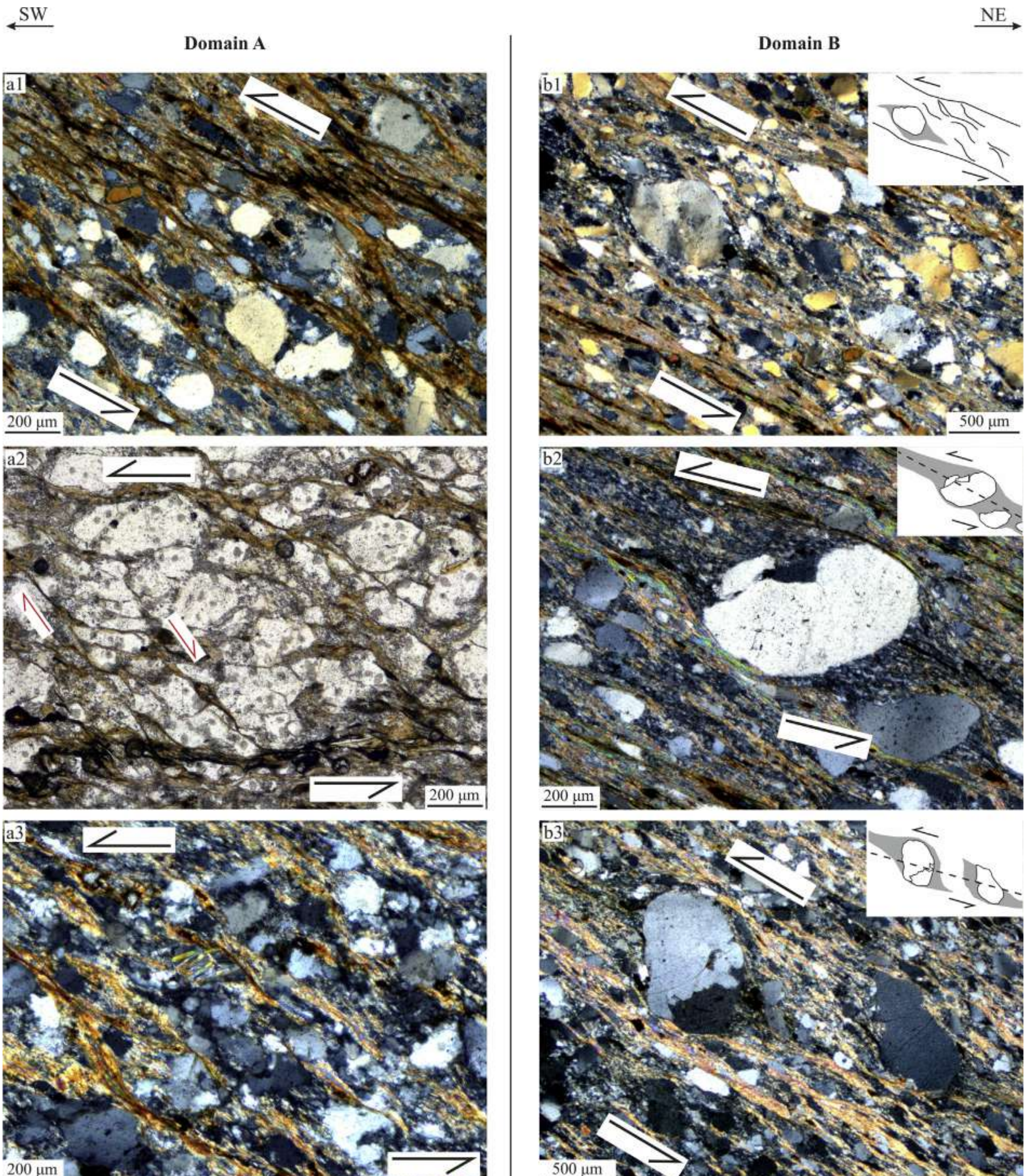

Fig. 3. Comparison of microstructures in domains A and B. Sub-figures a1, a2, a3 are from domain A, and b1, b2, b3 are from domain B. In all the figures NE is to the right. **(a1)** Quartz porphyroclasts embedded in finer matrix. The shear planes are present in the matrix and don't cross cut the quartz grains. The marginal recrystallisation of the quartz grains and the presence of clays along the shear planes are to be noted. Cross polarized light. (**a2)** Alignment of clays and mica represent the overall shear pattern of the rock. Red half arrows: antithetic shear. A coarse quartz grain fragmented into several sigmoid grains. Plane polarized light. **(a3)** Undulose extinction and marginal recrystallization of quartz. Cross polarized light. **(b1)** Strong mylonitic foliations, curved shear planes in the quartz rich part, neocrystallisation at the grain boundaries, undulose extinctions are to be noted. Cross polarized light. **(b2)** Symmetric pressure shadows (review in Mukherjee, 2017) formed at two sides of a quartz grain. Cross polarized light. **(b3)** σ-shaped tails near quartz clasts document shearing (black half arrows). Intra-granular healed fracture and the sutured sub-grain boundary in the central grain are to be noted. Cross polarized light. (For interpretation of the references to colour in this figure legend, the reader is referred to the Web version of this article.)

fragmentation of grains (Fig. 5). Alignment of fluid/solid inclusions along healed micro-cracks (Fig. 3a2, b2), which can be called a kind of "Tuttle lamellae" (review in Anders et al., 2014), also signifies the same. Symmetric- (Fig. 3b2) and asymmetric mantled porphyroclasts (Fig. 3b3) connote pressure solution and re-deposition of materials. Whereas, bulging in grain boundary (Fig. 3a1), neo-crystallization along grain boundaries (Fig. 3a3, b1) indicate bulging recrystallization (300–400 °C).

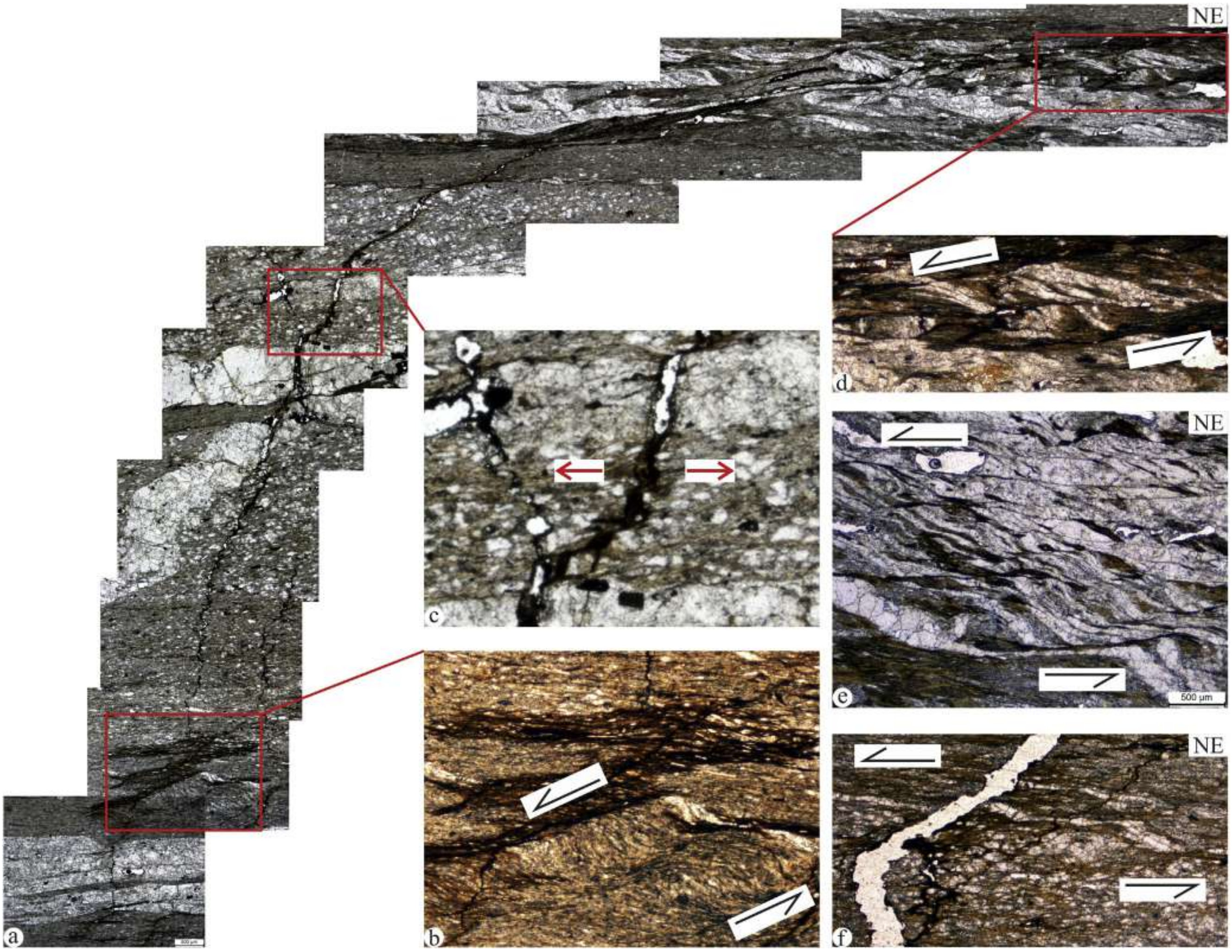

Fig. 4. Extensional-/dilatant shear fracture noted in XZ-section of domain-A. All figures in plane polarized light. **(a)** Mosaic showing the overall appearance of the fracture. In the central and lower part of the mosaic, where the quartz porphyroclasts are more abundant, the fracture is present at high-angle displaying shear-sense. Towards the upper part of the mosaic, where fine grained matrix and sheared quartz veins are present, the fracture gradually becomes parallel to the shear P. Width of each of the images is ~3.5 mm. **(b)** Shear fabric (shear sense: black half arrows) in finer matrix. Younger extensional fracture as in mosaic 'a' cuts it across. **(c)** Note the wide opening (probable extension direction: red half arrows) and stepping of the fracture. **(d)** Top-to ~ SW fore-sheared (black half arrows) quartz veins cross-cut by younger fractures. **(e)** Observations resembling '**d**' made from another part of the thin-section. **(f)** Fore-sheared (black half arrows) quartz veins cross-cut by younger extensional fractures. Both the features were generated by the same shear sense. Width of image ~3.5 mm. (For interpretation of the references to colour in this figure legend, the reader is referred to the Web version of this article.)

3.4. Rheological issues

The studied rock samples show evidences of intense ductile deformation, viz. sheared veins and foliations, pressure shadows, S-C fabrics etc. The rheology of a sheared rock-whether Newtonian or not-may be inferred from microstructures. For example, mantled porphyroclasts can show eye-shaped separatrix, absence of stair stepping in wings for Newtonian flow (review in Mukherjee, 2017) and bow-tie shaped separatrix, stair stepped wings for the non-Newtonian pattern (Passchier and Sokoutis, 1993; Passchier, 1994). However, the type of separatrix also depends on various other factors, viz., the aspect ratio of the porphyroclast, ratio of pure shear to simple shear etc. (Pennacchioni et al., 2000; Mandal et al., 2001).

Ductile deformation of rocks following Newtonian viscous behaviour is characterized by grain boundary sliding by diffusion mass transfer and grain boundary dislocation mechanisms. Ductile deformation of rocks following Non-Newtonian behavior reflect dominantly crystal slip plasticity by recovery processes, including dislocation climb and pile-up, sub-grain rotation and marginal recrystallization (Dimanov et al., 2015). Marginal recrystallisation was observed from both the samples (Fig. 3). Also, stepped (sigma-structure in Fig. 3b3) as well as non-stepped (symmetric clasts in Fig. 3b2) tails are associated with the porphyroclasts. This indicates roughly a Newtonian rheology for the samples from domains A and B.

Evidences of brittle deformation, e.g., presence of meso-scale Y-and P-planes and inter-/intra-granular micro-fractures, have also been noted in the samples from both the domains (Figs. 4 and 5). Brittle deformation is more preferred in the upper crustal rocks, whose rheological behavior can be approximated convincingly as linear elastic (Pollard and Fletcher, 2005; Turcotte and Schubert, 2014). Fracture mechanics presumes linear elastic behavior of rocks to investigate fracture propagation, the stress distribution at fracture tips, and cause of different fracture patterns (Irwin, 1960; Mandl, 2005; Stoeckhert et al., 2015). But, Gudmundsson (2011) argues that such an assumption is valid for < 1% of strain. Karato (2008), however, categorized both brittle- and plastic deformations under non-elastic deformation.

On the other hand, considering the co-existence of both ductile and brittle features, a visco-elastic rheology can be assigned for these rocks. Visco-elastic material, behaves as an elastic solid for short time-scales, but on geologic time scales (10^4yr) it acts a viscous fluid (Turcotte and

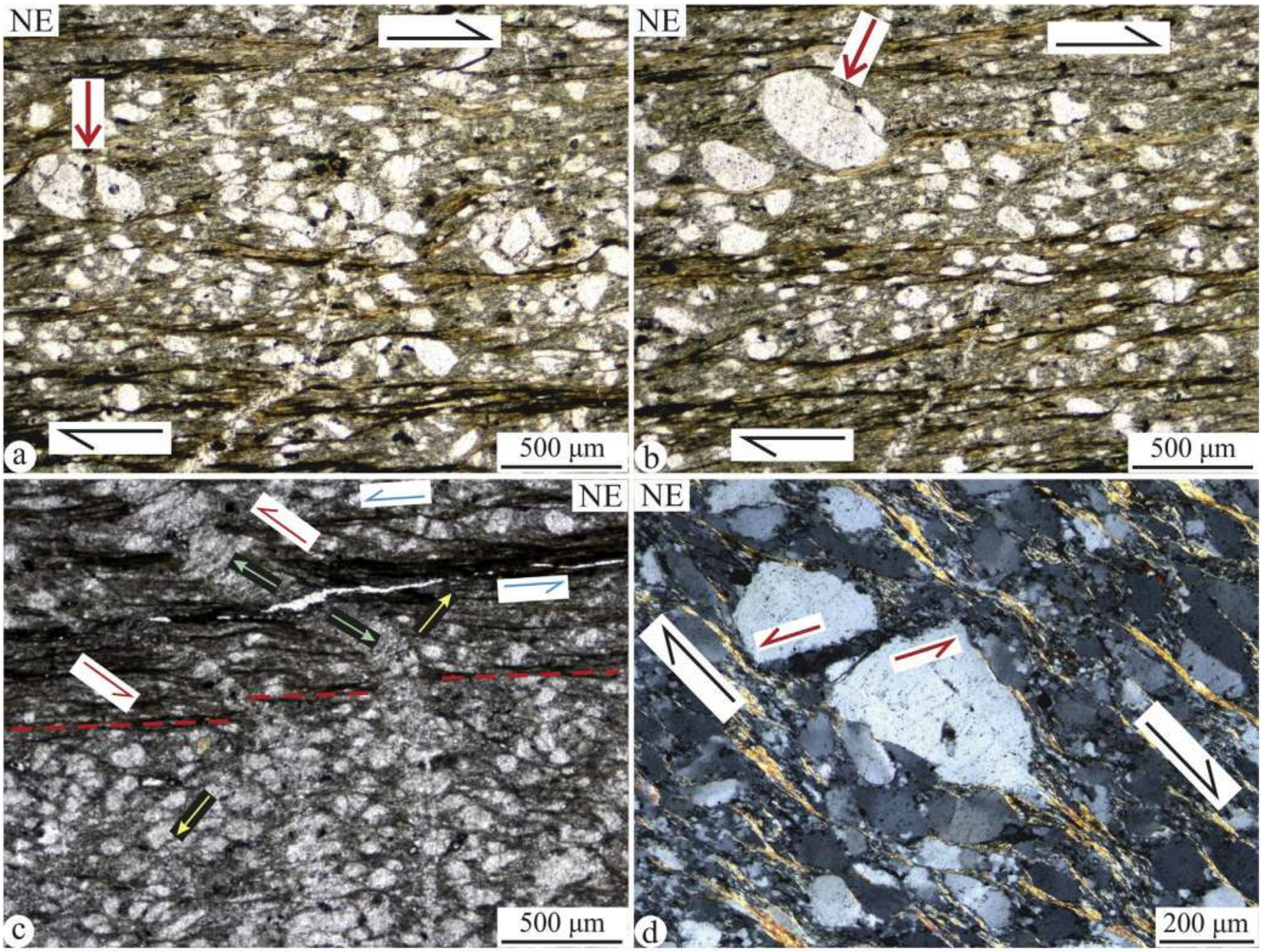

Fig. 5. Compressional and extensional features in XZ-section of domain-B. Black half-arrows indicate overall shear sense. **(a, b)** Clays and flaky minerals define the Y- and P- planes, which indicate compressional fore shear. The pull-apart (Hippertt, 1993; Mukherjee, 2010) features (red full arrow) indicate extension. **(c)** The vein is sheared with a minor drag along them (red half arrows). This shear sense matches with the top-to-SW sense as seen in the whole rock (blue half arrow). The extension direction for the sheared quartz vein (yellow arrows) is at a high-angle with a younger tensile crack that crosscuts it (green full arrows). Plane polarized light for **a, b, c. (d)** Antithetic brittle extensional sheared (red half arrows) quartz porphyroclast in a foreshear (black half arrows) regime. Cross polarized light. (For interpretation of the references to colour in this figure legend, the reader is referred to the Web version of this article.)

Schubert, 2014; Fossen, 2016). Such materials are more suitable to model the lower crust deformations. In the present context, both the viscous and the elastic features might be correlated with the active aseismic-seismic cycles going on in this region of high seismicity (Rajendran et al., 2017 and references therein).

4. Finite strain analysis and vorticity measurement

4.1. Strain markers

Elliptical quartz grains are widely used strain marker as they record the deformation process through the change in shape (e.g., Xypolias and Koukouvelas, 2001). The plastically deformed quartz grains are selected for the R_f-φ analyses. Whereas, for vorticity analysis, rigid quartz grains with pressure shadows (from domain B) were used. Strain analyses involve several assumptions (Xypolias, 2010 and references therein; Sengupta and Chatterjee, 2015). We discuss them below taking examples from our samples.

1. The studied rock samples show Newtonian rheology (Section-3.4), which is a prerequisite for the strain and vorticity analyses.
2. Recrystallized and fractured grains should not be analyzed since their strained shapes get modified by those processes. Clasts should be freely-rotating rigid ellipsoids, perfectly bonded to the matrix and ought not mutually interact mechanically. Strain partitioning at the clast interface should be avoided. In GSZ thin sections, both elliptical and non-elliptical types of clasts exist within a fine-grained matrix (Fig. 3), which validates the rationale for strain analyses. Grains that are either fractured or are in mutual contact were avoided, and semi-elliptical/irregular shaped isolated unfractured grains were selected in this study.
3. The thin-section should be orthogonal to the rotation axis of the porphyroclasts, otherwise the methods will underestimate the mean kinematic vorticity number (W_m). This also happens when the sample lacks grains with large aspect ratios (R_f). W_m is over-estimated if the clasts did not attain a stable position. Well-developed δ-type clasts or plots with sharp cut-off points (in the R_f-φ diagram) signify that the strain was sufficient enough for the grains to stablilize. Following these cautions, The XZ-sections (perpendicular to the strike of the Y-plane) from both the domains were used in the present study. In our study, the chosen clasts have overall a wide range of aspect ratios: 1.00–4.65 in domain-A, and 1.02–5.94 in domain-B.

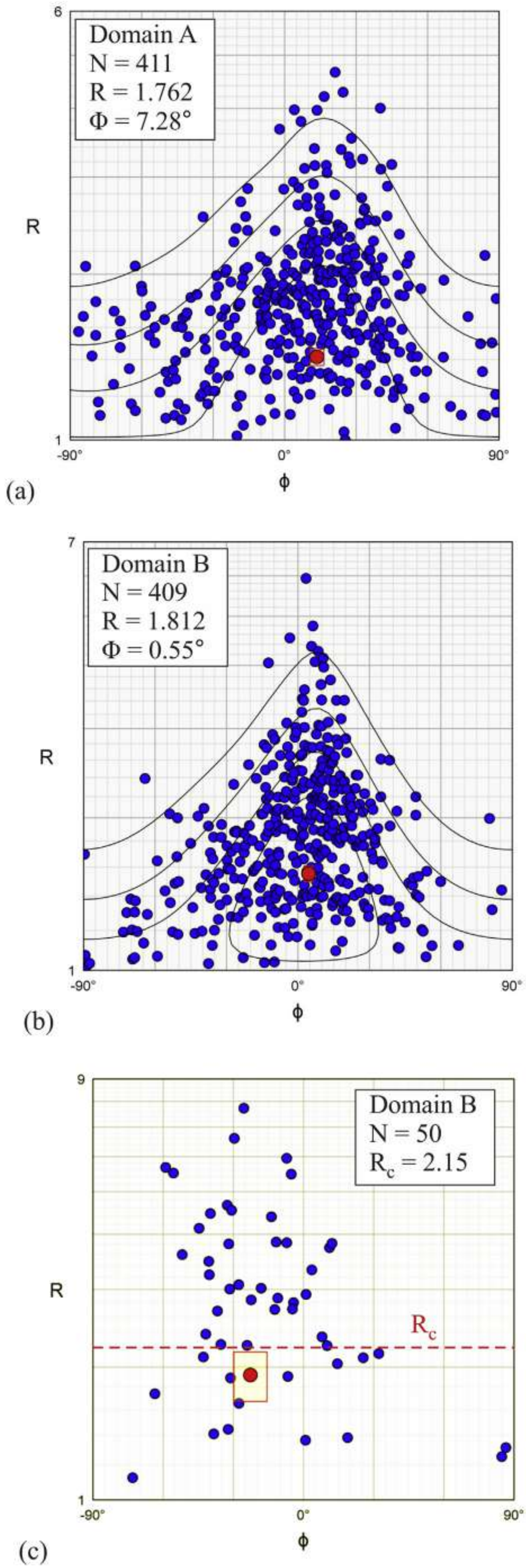

Fig. 6. Strain analyses and KVN measurements. Red dot: Mean values of R (i.e., R_f) and φ. **(a, b)** R_f-φ analyses results for domains A and B, respectively. **(c)** Kinematic vorticity number calculation by PAR method for domain B. Red broken line indicates the cut-off point and R_c is the corresponding R value. (For interpretation of the references to colour in this figure legend, the reader is referred to the Web version of this article.)

4.2. Method

The R_f-φ method (Dunnet, 1969; Lisle, 1985) is commonly used to analyze strain. R_f is the ratio of the lengths of major-to minor axes of the ellipse, and φ is the angle between the major axis of the ellipse and a reference direction, which is usually the primary shear direction. The R_f-φ values were obtained for ~ 410 grains from each of the thin-sections prepared. From these values, the R_f-φ graphs were plotted and the vector mean of φ and the harmonic mean of R_f were calculated.

The Kinematic Vorticity Number (KVN; Hanmer and Passchier, 1991; review in Xypolias, 2010) indicates coaxiality of the successive deformation stages and quantifies the % of pure- and simple-shears. Amongst the various approaches, the Porphyroclast Aspect Ratio (PAR; Passchier, 1987) method uses strained elliptical clasts to measure the KVN. A critical value of R (R_c) is marked on the Rf-φ graph (e.g., Fig. 8c of Xypolias, 2010) to mark the cut-off point. From the R_c value, the mean KVN (W_m) is calculated (eqn. (1)).

$$W_m = (R_c^2 - 1)/(R_c^2 + 1) \quad (1)$$

4.3. Results

The EllipseFit v3.3.0.62 software was used to generate the 'R_f-φ' diagrams. R_f values of 1.762 and 1.812 were obtained from domains-A (Fig. 6a) and –B (Fig. 6b), respectively. The calculated KVN for domain B is 0.65 (Fig. 6c), indicating ~55% pure shear. Such a combination of pure- and simple-shear is common in natural shear zones (e.g., Fossen and Cavalcante, 2017; Long et al., 2017) and indicates that the rock would eventually fail by dilatant shear fractures/hybrid fractures (Ramsey and Chester, 2004; Ishii, 2015).

5. Grain size analyses

Areas of 410 quartz porphyrocalsts from both the domains- A and B were measured (Fig. 7) using the software JMicroVision v1.2.5. The grain size for domain A is < 40,000 μm^2. Whereas, significant amount of coarser grains (> 45,000 μm^2) are present in the domain-B. Whether this is the major guiding criterion behind the selective formation of sigmoid brittle-shear planes (P-planes) in domain-B, is addressed in the following numerical modeling.

6. Numerical modeling

6.1. Theory & background

Brittle fracturing of rocks, the associated stress-strain distribution as well as the factors responsible for their initiation and propagation, have been widely studied with the help of numerical simulations (e.g., Camacho and Ortiz, 1996; Hoek and Martin, 2014 and references therein; Zhang and Zhao, 2014; Gao et al., 2016; Hattori et al., 2017; Wu et al., 2017). Although, most of the previous studies considered elastic-plastic, visco-elastic or visco-plastic rheological models to investigate brittle deformations (e.g., Sandiford et al., 2006; Behn et al., 2007; Kaus, 2010; Roland et al., 2010; Currenti and Williams, 2014; Ding and Lin, 2016; Thompson and Parsons, 2016), purely elastic rheological model was preferred by many as well (e.g., Burchardt, 2008; Xu et al., 2012; Lu et al., 2014; Guallini et al., 2015; Wei et al., 2015; Nabavi et al., 2017).

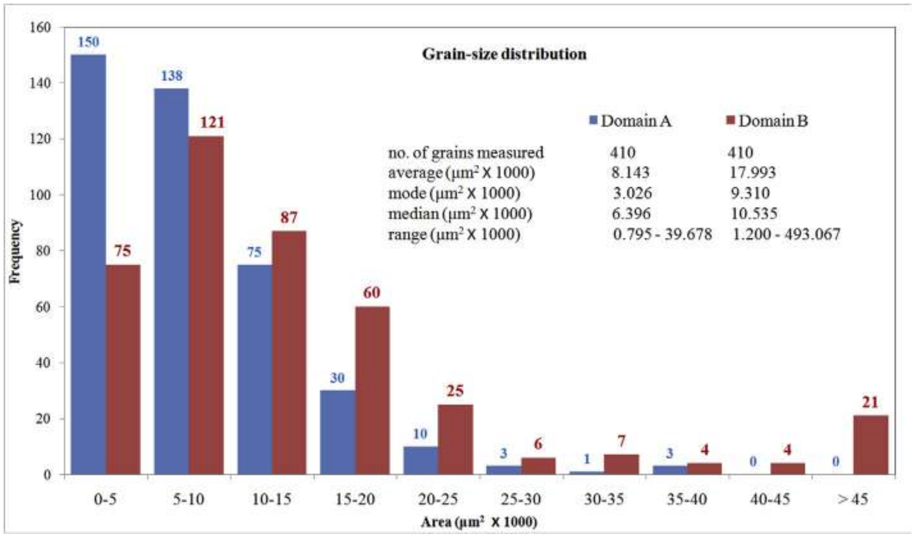

Fig. 7. Grain-size distribution from domains -A and -B. Grain sizes were measured using JMicroVision software (v 1.2.5).

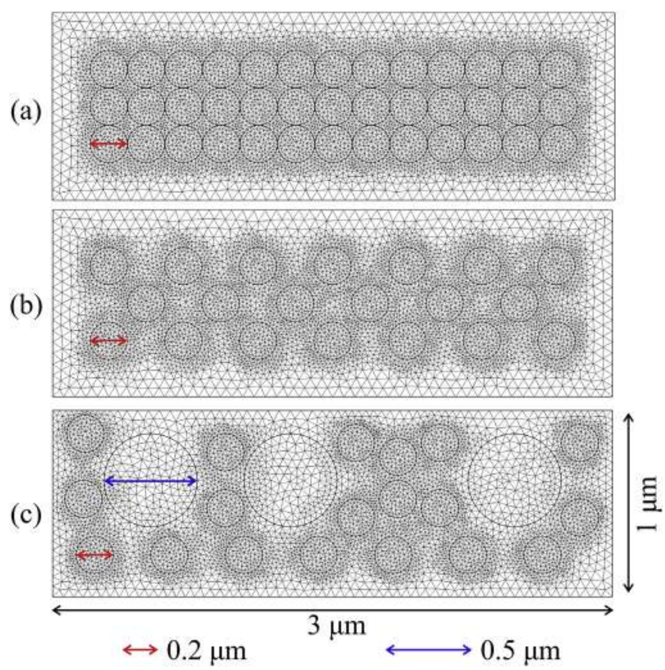

Fig. 8. Geometry of the model domains and the meshing. **(a)** Model-1, **(b)** Model-2 and **(c)** Model-3.

This study represents an approximation to the more realistic non-linear deformation processes of the upper crust. Hence, an isotropic, linear elastic behavior was chosen for the materials incorporated in our models. Brittle deformation of rocks can be studied with the help of either the Drucker-Prager or the Mohr-Coulomb failure criterion (Hobbs and Ord, 2015). The former is often approximated as a '*smoothed version*' of the latter in a 3D scenario/model (Tetreault and Buiter, 2012; Currenti and Williams, 2014; Cervera et al., 2016; Carcione et al., 2018).

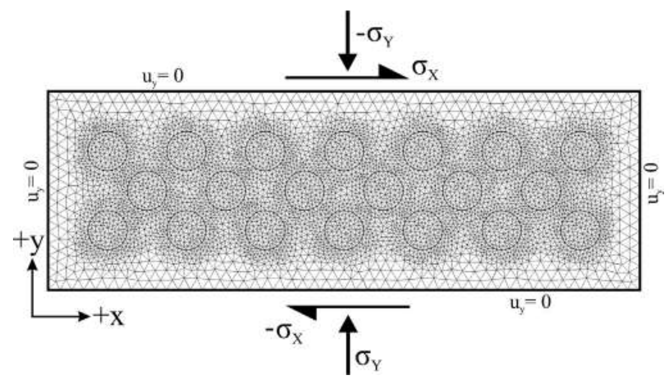

Fig. 9. Stresses applied on the upper and lower boundaries of the model domain. Negative sign implies that the stress is directed towards the negative side of the X- or the Y-axes.

6.2. Governing equations

Equations (2)–(4) must be solved to determine the state of stress and displacements at the end of a 2D quasi-static deformation of an isotropic and linear elastic material.

$$\sigma_{ij} = \lambda\delta_{ij}\sum_{k}\varepsilon_{kk} + 2\mu\varepsilon_{ij} \quad \text{Hooke's law} \tag{2}$$

$$\nabla\cdot\sigma + F = 0 \quad \text{static equilibrium} \tag{3}$$

$$\varepsilon = \frac{1}{2}[\nabla u + (\nabla u)^T] \tag{4}$$

Table 1
Physical parameters of the materials used.

Material	Density (kg m^{-3})	Young's Modulus (GPa)	Poisson's Ratio (unitless)	Cohesion/Inherent shear strength (MPa)	Angle of Internal friction (radian)
Sandstone	2000–2800[1,2]	10–60[1,2]	0.1–0.3[1,2]	25.5–27.2[3,4]	0.46–0.6[1,5]
Quartzite	2500–2700[1,2]	40–60[1]	0.15–0.20[1]	70.6 [4,6]	0.45–1.05[1,5]

References: 1. Gudmundsson (2011), 2. Henderson and Henderson (2009), 3. Zhang et al. (2008), 4. Goodman (1980), 5. Pollard and Fletcher (2005), 6. Takahashi and Tanaka (2017). Note: the mean values of the ranges are used in our models, except for the cohesion for quartzite where a single value is obtained from the literature.

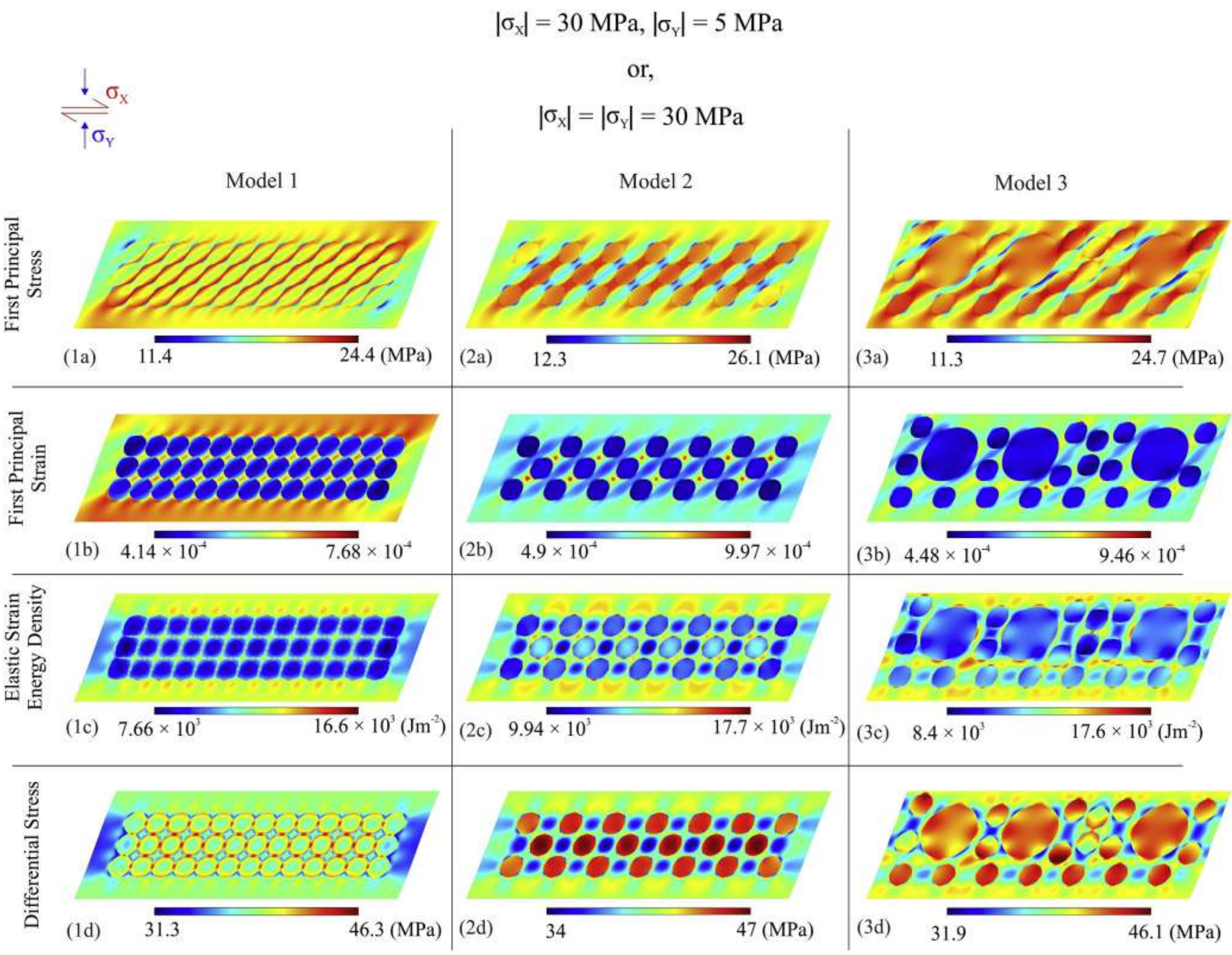

Fig. 10. Variations in the response of the three models to general shear, where $|\sigma_X| > |\sigma_Y|$ or, $|\sigma_X| = |\sigma_Y$. Joule meter^{-2} is the unit of surface tension or stiffness.

where, $\boldsymbol{\sigma}$ (stress matrix) = $\begin{bmatrix} \sigma_{xx} & \sigma_{xy} \\ \sigma_{yx} & \sigma_{yy} \end{bmatrix}$; ε (strain matrix) = $\begin{bmatrix} \varepsilon_{xx} & \varepsilon_{xy} \\ \varepsilon_{yx} & \varepsilon_{yy} \end{bmatrix}$ = $\begin{bmatrix} \frac{\partial u}{\partial x} & \frac{1}{2}\left(\frac{\partial u}{\partial y} + \frac{\partial v}{\partial x}\right) \\ \frac{1}{2}\left(\frac{\partial v}{\partial x} + \frac{\partial u}{\partial y}\right) & \frac{\partial v}{\partial y} \end{bmatrix}$; ∇u (displacement gradient) = $\begin{bmatrix} \frac{\partial u}{\partial x} & \frac{\partial u}{\partial y} \\ \frac{\partial v}{\partial x} & \frac{\partial v}{\partial y} \end{bmatrix}$; λ and μ are Lamé constants; and δ_{ij} (Kronecker delta) = $\begin{cases} 1, & if\, i = j \\ 0, & if\, i \neq j \end{cases}$; F is the body force (Bahat et al., 2005; Jaeger et al., 2009; Karato, 2008; Gerya, 2010; Newman, 2012; Perez, 2017).

The effect of intermediate principal stress (σ_2) on brittle failure is only considered by the latter (Jaeger et al., 2009). Colmenares and Zoback (2002) showed that failure criteria such as Mohr-Coulomb or Hoek-Brown, which ignores the influence of σ_2, can be used. Shear failures, the focus of this study, are best anticipated by the Mohr-Coulomb criterion (eqn. (5); Paterson and Wong, 2005; Bai and Wierzbicki, 2010; Cox, 2010; Kaiser and Kim, 2015):

$$\sigma_1\{\sqrt{(1 + \mu_i^2)} + \mu_i\} - \sigma_3\{\sqrt{(1 + \mu_i^2)} - \mu_i\} - 2S = 0 \quad (5)$$

where, σ_1: maximum principalstress; σ_3: minimum principal stress; μ_i: coefficient of internal friction and S: inherent shear strength or cohesion (Pollard and Fletcher, 2005; Jaeger et al., 2009). Being representative of the Lesser Himalayan section, the GSZ is a part of the India-Eurasia collisional-compressional domain (e.g.,Mukherjee et al., 2015). Hence, the X-axis and the σ_1 orients NE-SW, the Y-axis and the σ_3 is vertical, and the σ_2 is orogen parallel, i.e., NW-SE.

Eqn. (5) was used to determine the locations susceptible to shear fracture. With the help of finite element numerical simulations, the values of the expression on the left hand side of eqn. (5) (Yield Function: Y_F) was determined throughout the model domain. Cohesion (S) in eqn. (6) is also related to the uniaxial compressive strength (C_U) and coefficient of internal friction (μ_i) of the material (Pollard and Fletcher, 2005):

$$S = \frac{C_U}{2\{(\sqrt{(1 + \mu_i^2)}) + \mu_i\}} \quad (6)$$

Previous authors have often incorporated a combination of Mohr-Coulomb and tensile failure criteria to model/study brittle deformation (Wilson et al., 2007; Lunn et al., 2008). As per Zhu and Tang (2002) and Jaeger et al. (2009), macroscopic shear failures often involve tensile damage at smaller scales. However, in our model such a combination was neglected for simplification purposes, and hence tension cut-off has not been included.

6.3. Model setup

We ran three 2D models: 1, 2, and 3 (Fig. 8). Each of them consists of circular quartz grains within a rectangular (1 μm × 3 μm) sandstone matrix (rheological parameters in Table 1). In model 1 (Fig. 8a), the sizes of all the quartz grains are identical: 0.2 μm diameter. They are

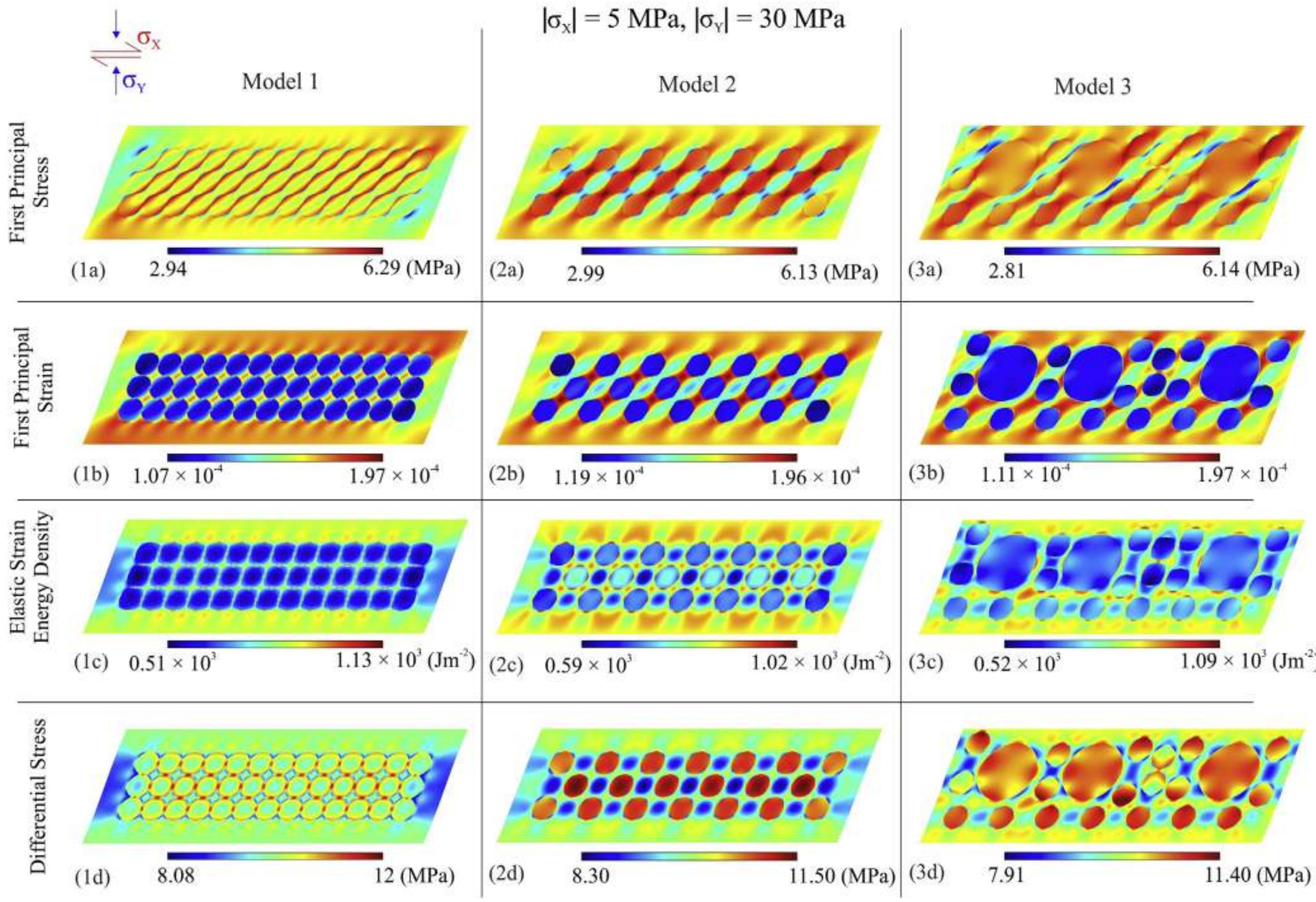

Fig. 11. Variations in the response of the three models to general shear, where $|\sigma_X| < |\sigma_Y|$.

densely packed with mutual point contact. In Model 2 (Fig. 8b), the grainsize is same as in model 1, however, unlike model 1, the grains are not in contact with their neighbours. The closest distance between two adjacent grains is ~0.28 μm. Model 3 (Fig. 8c) contains grains of two different sizes. Larger grains have a diameter of 0.5 μm. The size of the smaller grains is same in model 1 and 2. But, the largest distance between the two neighbouring small grains is 0.4 μm in model 3. As in model 2, none of the grains of model 3 are in mutual contact. Models 1, 2 represent domain A, and Model 3 domain B.

In our numerical analyses, eqns. (2–4) were solved using the finite element method (Courant, 1943; McHenry, 1943; Zienkiewicz and Taylor, 2000) in COMSOLMultiphysics v5.0 software. As in most of continuum numerical models, the materials in this study were considered to be (nearly) incompressible (Buiter, 2012). Dilation due to shear was not considered. For quasi-static set up, the imposed acceleration as well as the kinetic energy of the system (both generated due to application of stress) were neglected (Buiter, 2012; Hobbs and Ord,2015). Now given that this is a time-independent study, results are independent of the inertial parameters. We chose triangular mesh in 2D finite element (FE) models, as practiced widely (Pepper and Heinrich, 2006; Frey and George, 2008; Ismail-Zadeh and Tackley, 2010; Tadmor et al., 2012; Fenner, 2013). COMSOL consists of automatic mesh generation module, which discretizes both the matrix and clast domains into triangular elements, with advancing front tessellation (Zhang, 2016 and references therein). The element concentration is higher at the clast boundaries since the sizes of meshes reduce close to the curved boundaries.

The coordinate axes X and Y are as per Fig. 9. Assuming a plane strain, all the models were subjected to general shear. σ_X denotes the shear stress parallel to the X-axis on the two length boundaries of the rectangle, and towards opposite directions. Compressive stress σ_Y apply parallel to the Y-axis on the same boundaries. The velocity components along the Y-direction (u_y) were restricted to zero (no velocity boundary condition) for all the four edges of the rectangle, in order to inhibit rotation of the geometry during deformation (Johnson et al., 2009; Nabavi et al., 2017 and references therein). For the sake of simplicity, the effects of grain size reduction with deformation were avoided. Our models also presume that, unlike the natural case referred by Warren and Hirth (2006), no strain partitioning took place.

We ran two different experiments on models 1–3. In the first experiment (Experiment 1) models 1, 2 and 3 were subject to three different stress conditions: *i.* The layer parallel shear stress (σ_X) = 30 MPa, the layer normal stress (σ_Y) = 5 MPa; *ii.* $\sigma_X = \sigma_Y$ = 30 MPa; *iii.* σ_X = 5 MPa, σ_Y = 30 MPa. The aim of Experiment 1 is to check the effects of variable grain sizes on various parameters, such as First Principal Stress, First Principal Strain, Elastic Strain Energy Density (ESED) and the Differential Stress. In another experiment (Experiment 2), identical stresses were applied to the three models with $|\sigma_X|$ = 390 MPa and $|\sigma_Y|$ = 120 MPa. Experiment 2 was conducted to understand the effect of variable grain size and distribution on the spatial distribution of the brittle shear planes/fractures, P-plane in particular. We also test the dependency of the failure pattern on grain-size variation and distribution.

6.4. Results and interpretations

6.4.1. Experiment 1

The behavior of the models under different σ_X and σ_Y conditions have been presented in Figs. 10 and 11. For $\sigma_X = \sigma_Y$ and $\sigma_X > \sigma_Y$, the models 1–3 generated identical results. The results show that, larger the

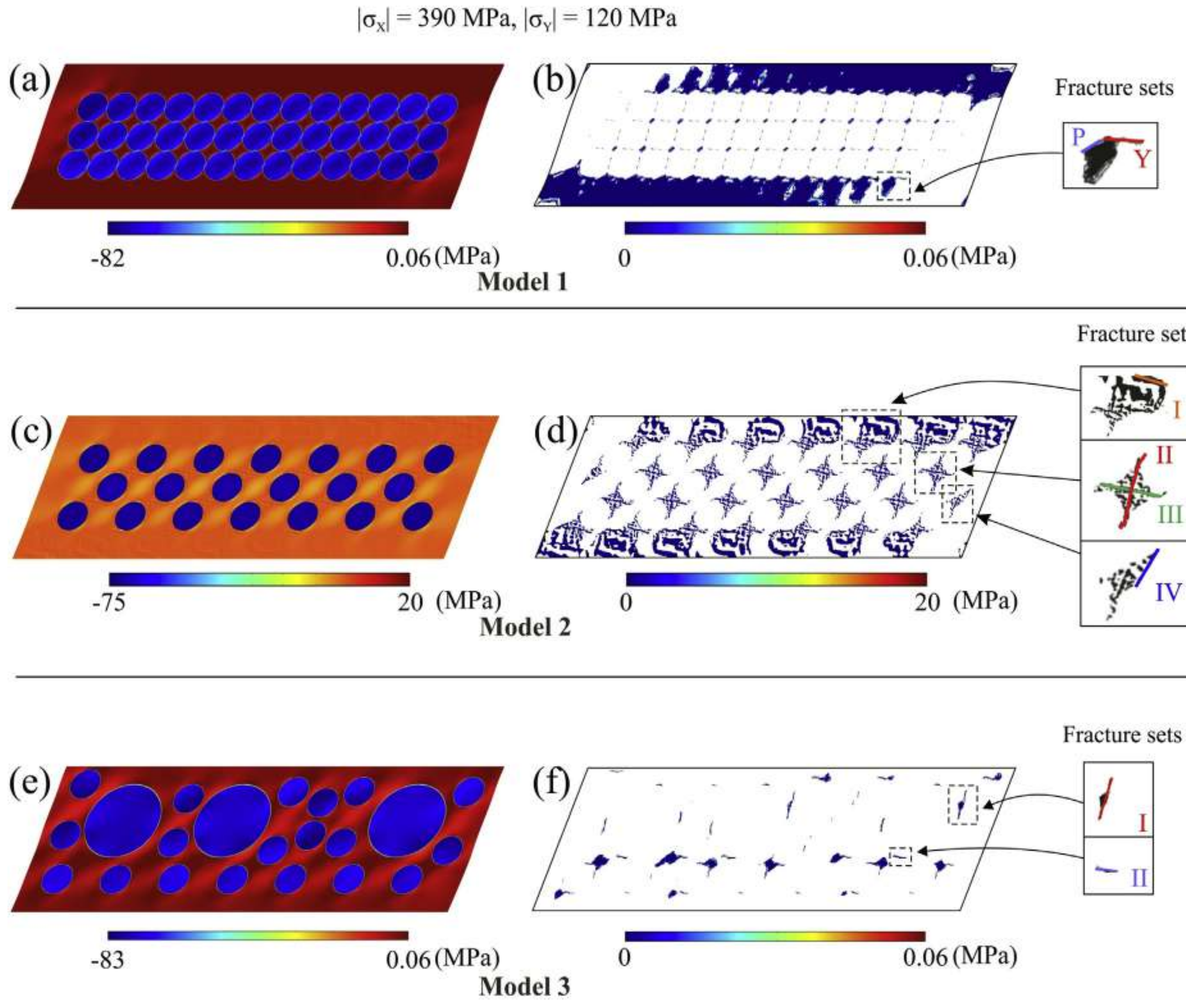

Fig. 12. Values of the yield function (Y_F; right hand side expression in eqn. 5) throughout the domains after deformation. $|\sigma_X|$ & $|\sigma_Y|$: magnitude of force per unit length applied on the upper and lower boundaries of the rectangular domain, parallel to X- and Y-axes respectively. (a, c, e) show total range of yield function (Y_F) throughout the model domains. The images of the right column (b, d, f) show only those zones where the values of the $Y_F \geq 0$. The inset diagrams represent the zoomed version of the corresponding sub-domains. The types of fractures have also been marked.

grain-size, lower the overall rock ESED. The ESED and differential stress is lowest in Model 1, where the quartz grains are in contact. The grains in contact behave as a lager grain of cumulative size. Models 2 and 3 show that the presence of quartz grains decreases the ESED of the inter-granular spaces.

6.4.2. *Experiment 2*

Shear fractures are more likely to develop at places with $Y_F \geq 0$ (Pollard and Fletcher, 2005; Gudmundsson, 2011). Value of Y_F varies from −83 MPa to 20 MPa in our models (negative symbol indicates absence of shear fracture). The solutions obtained, show that in case of Model-1, the curved shear-fractures are mostly restricted outside the area occupied by clasts. In other words, they do not pass through/cut across the grains. This is also seen in the domain A microstructures (Fig. 3a1). Also, the acute angle between the fractures and the possible Y-shears, increase from ~32° close to the clasts to ~61° near the boundary of the model domain (Fig. 12a). The ones at < 45° to the horizontal (Y-shear) are possibly the P-planes (Meyer et al., 2017). On the other hand, for Model-2, four sets of shear fractures develop (Fig. 12b). Close to the domain-boundary, the Set-I fractures form at ~40° with the horizontal (domain boundary). Whereas in between the grains fractures are restricted to somewhat rhombic domains, whose diagonals define another two sets of fractures: one of which is at high angle (Set II ~ 78°) and the other one being sub-parallel (Set III), to the horizontal (Fig. 12c and d). Similar shear fractures are observed in Fig. 3. Also, near the two lateral domain-boundaries another set of fractures Set IV (~ 50° to Y-plane), are produced (Fig. 12b). These shear fractures appear to be more straight than those in Model-1. Model-3, however, shows two sets of shear fractures. One set, possibly the R′shear plane form at ~77° to the Y-plane (domain boundary) and the other set at ~ 48° The second set is present in between the clasts or between the clasts and the domain-boundary. Whereas, the high-angle ones are restricted near the lateral boundaries (which were parallel to Y-axis before deformation) of the model (Fig. 12c). Domain-B does show under microscope two sets of shear fractures: one at a high-angle to the Y-plane (possibly the P-plane) and the other at a gentler angle (Fig. 5a).

7. Discussions

In the field, the two domains- A and B are merely about a meter away. Both the domains have same mineralogy and display similar strain. Hence the domains can be considered to have experienced the same deformation throughout the geological time. Under microscope, both the domains show prominent signatures of phyllonitisation (Figs. 3 and 5; Wenk and Pannetier, 1990; Goodwin and Wenk, 1995) such as: *(i)* close-spaced phyllosilicate-rich shear planes; *(ii)* fragmentation of coarser grains; and *(iii)* intense preferred orientation of mainly flaky minerals, e.g., micas. Profound fluid activities and presence of clays discriminate phyllonites from mylonites and cataclasites (Mancktelow and Pennacchioni, 2004; Jefferies et al., 2006). However, the mylonitic foliations are better developed/preserved in domain B. At the same time, micro-fractures present in the domains are dissimilar. Clay-rich extension fractures persist in the domain-A. Sample from domain-B dominantly exhibit intra-granular fractures (red arrows in Fig. 5b and c). Inter-granular fractures, though present, are much less in number and filled with quartz. The key difference between the domains were pointed out by the grain-size analysis (section 5), which shows a broader range of grain-size distribution in domain-B. This broader grain-size distribution enhanced diffusion creep in domain-B, and more importantly suppressed the effects of dislocation creep (Montési and Hirth, 2003). The observed differences in the two domains, from the presence of P-planes in field exposure to the discussed micro-structures, can be explained in this way.

General shear with equal kinematic vorticity numbers deciphered from the two domains indicate that the studied rock exposure underwent similar proportion of pure- and simple shear (section 4). Therefore, the numerical models utilize stresses both perpendicular and parallel to the Y shear planes. The domains have almost identical mineralogy and strain pattern. But, domain-B has larger sizes of quartz porphyroclasts, which has significantly reduced the overall strain of the body (Figs. 10 and 11). Finite element modeling clearly reveals similar dependence of spatial distribution of shear fractures on grain-size variation. P-planes are more prominent in Models- 2 (equigranular, isolated; equivalent to domain-A) and 3 (coarser grains, isolated; equivalent to domain-B). Moreover, coarser grain-size results in two sets of shear fractures, one at a high-angle to the domain-boundary, and another much lower angle. Interestingly, the P-planes develop earlier than the Y-planes in all the models. Similar conclusions came from other terrains (Skempton, 1966; Bartlett et al., 1981; Kirkwood and Malo, 1993) in meso-and micro-scale, but modeling remained due. Unlike that in Models- 2 or 3, the P-shear fractures in Model 1 (equigranular, close packed; equivalent to domain-A) are curved. The elastic strain energy density of those models shows that the coarser part has less energy and prefers to remain less deformed than the finer part. Hence, the coarser part of the natural exposure (domain-B) seems less strained under similar condition.

8. Conclusions

Through this study, the effect of grain size on brittle failure has been examined in naturally deformed samples and the following observations have been made:

1. Two domains were demarcated in the field exposure based on the presence of brittle P-planes.
2. XRD analyses and thin-section observations indicate that rocks in the two chosen domains have same mineralogy. Therefore, development of P-planes preferentially in one of those domains cannot arise from mineralogical disparity. Strain analyses further shows that both the domains underwent similar general shear deformation.
3. The grain size analyses shows that domain-B has coarser grains of quartz than that in domain-A. This broader grain-size range decreased/delayed the effects of dislocation creep in domain B. Numerical models further indicate that, presence of coarser grains reduces the elastic strain energy density. These explain why the domain-B is devoid of P-planes in meso-scale.

Acknowledgements

Fieldwork was funded partially by IIT Bombay in terms of CPDA grant to SM, and partly through NB's University Grants Commission (Govt. of India), Junior Research Fellowship: F.2-2/98(SA-1). Kanchan Pande and George Mathew commented NB's internal oral presentations in the Dept. Trupti Chandrasekhar (IIT Bombay) assisted the XRD analyses. SM was supported by a research sabbatical in 2017. Review comments by Paris Xypolias and an anonymous reviewer significantly improved the manuscript. The authors acknowledge the efforts of the Associate Editor, Ian Alsop.

Appendix A. Supplementary data

Supplementary data related to this article can be found at http://dx.doi.org/10.1016/j.jsg.2018.03.010.

References

Agarwal, N.C., Kumar, G., 1973. Geology of the upper Bhagirathi and Yamuna valleys, Uttarkashi district. Kumaun Himalaya. Himal. Geol. 3, 2–23.
Anders, M.H., Laubach, S.E., Scholz, C.H., 2014. Microfractures: a review. J. Struct. Geol. 69, 377–394.
Bahat, D., Rabinovitch, A., Frid, V., 2005. Tensile Fracturing in Rocks: Tectonofractographic and Electromagnetic Radiation Methods. Springer, New York, pp. 570 ISBN 978-3-540-26614-3.
Bai, Y., Wierzbicki, T., 2010. Application of extended Mohr–Coulomb criterion to ductile fracture. Int. J. Fract. 161, 1–20.
Bartlett, W.L., Friedman, M., Logan, J.M., 1981. Experimental folding and faulting of rocks under confining pressure Part IX. Wrench faults Limest. layers. Tectonophys. 79, 255–277.
Behn, M.D., Boettcher, M.S., Hirth, G., 2007. Thermal structure of oceanic transform faults. Geology 35, 307–310.
Buatier, M., Lacroix, B., Trincal, V., Charpentier, D., Labaume, P., Trave, A., 2013. Synkinematic phyllosilicates in a thrust fault zone: good proxy for PT conditions, deformation mechanism and mass transfers (example of the Monte perdido Thrust in southern Pyrenees). In: EGU General Assembly Conference Abstracts, vol. 15.
Buiter, S.J., 2012. A review of brittle compressional wedge models. Tectonophysics 530, 1–17.
Burchardt, S., 2008. New insights into the mechanics of sill emplacement provided by field observations of the Njardvik Sill, Northeast Iceland. J. Volcanol. Geotherm. Res. 173, 280–288.
Camacho, G.T., Ortiz, M., 1996. Computational modelling of impact damage in brittle materials. Int. J. Solids Struct. 33, 2899–2938.
Cappa, F., Rutqvist, J., 2011. Impact of CO2 geological sequestration on the nucleation of earthquakes. Geophys. Res. Lett. 38, L17313.
Carcione, J.M., Currenti, G., Johann, L., Shapiro, S.A., 2018. Modeling fluid-injection induced microseismicity in shales. J. Geophys. Eng. 15, 234.
Célérier, J., Harrison, T.M., Beyssac, O., Herman, F., Dunlap, W.J., Webb, A.A.G., 2009. The Kumaun and Garwhal lesser Himalaya, India: Part 2. Thermal and deformation histories. Geol. Soc. Am. Bull. 121, 1281–1297.
Cervera, M., Lafontaine, N., Rossi, R., Chiumenti, M., 2016. Explicit mixed strain–displacement finite elements for compressible and quasi-incompressible elasticity and plasticity. Comput. Mech. 58, 511–532.
Colmenares, L.B., Zoback, M.D., 2002. A statistical evaluation of intact rock failure criteria constrained by polyaxial test data for five different rocks. Int. J. Rock Mech. Min. Sci. 39, 695–729.
Cox, S.F., 2010. The application of failure mode diagrams for exploring the roles of fluid pressure and stress states in controlling styles of fracture-controlled permeability enhancement in faults and shear zones. Geofluids 10, 217–233.
Courant, R., 1943. Variational methods for the solution of problems of equilibrium and vibrations. Bull. Am. Math. Soc. 49, 1–23.
Currenti, G., Williams, C.A., 2014. Numerical modeling of deformation and stress fields around a magma chamber: constraints on failure conditions and rheology. Phys. Earth Planet. Interiors 226, 14–27.
Dimanov, A., Raphanel, J., Bornert, M., Bourcier, M., Gaye, A., Ludwig, W., 2015. Ductile shear zone rheology: the viewpoint of experimentally crept lower crustal rocks and analogues. In: EGU General Assembly Conference Abstracts, vol. 17. pp. 14297.
Ding, M., Lin, J., 2016. Deformation and faulting of subduction overriding plate caused by a subducted seamount. Geophys. Res. Lett. 43, 8936–8944.
Dubey, A., 2014. Understanding an Orogenic Belt: Structural Evolution of the Himalaya. Springer International Publishing, Switzerland, pp. 292–294.
Dunnet, D., 1969. A technique of finite strain analysis using elliptical particles. Tectonophysics 7, 117–136.
Fenner, R.T., 2013. Finite Element Methods for Engineers, second ed. World Scientific Publishing, London, pp. 245 ISBN-10: 1848168861.
Fjar, E., Holt, R.M., Raaen, A.M., Risnes, R., Horsrud, P., 2008. Petroleum Related Rock Mechanics, vol. 53. Elsevier, pp. 491 ISBN: 9780444502605.
Fossen, H., 2016. Structural Geology, second ed. Cambridge University Press, Cambridge, pp. 510 ISBN-10: 0521516641.
Fossen, H., Cavalcante, G.C.G., 2017. Shear zones–A review. Earth-Science Rev. 171, 434–455.
Fukuda, J.I., Shimizu, I., 2017. Theoretical derivation of flow laws for quartz dislocation creep: comparisons with experimental creep data and extrapolation to natural conditions using water fugacity corrections. J. Geophys. Res. Solid Earth 122, 5956–5971.
Frey, P.J., George, P.L., 2008. Mesh Generation: Application to Finite Elements, second ed. John Wiley &Sons, Hoboken, pp. 816 ISBN: 9781848210295.

Gao, F., Stead, D., Elmo, D., 2016. Numerical simulation of microstructure of brittle rock using a grain-breakable distinct element grain-based model. Comput. Geotechnics 78, 203–217.
Gerya, T., 2010. Introduction to Numerical Geodynamic Modelling. Cambridge University Press, Cambridge, pp. 345 ISBN 0521887542.
Gleason, G.C., Tullis, J., 1995. A flow law for dislocation creep of quartz aggregates determined with the molten salt cell. Tectonophysics 247, 1–23.
Goodwin, L.B., Wenk, H.R., 1995. Development of phyllonite from granodiorite: mechanisms of grain-size reduction in the Santa Rosa mylonite zone, California. J. Struct. Geol. 17, 689699–697707.
Goodman, R.E., 1980. Introduction to Rock Mechanics, vol. 2. John Wiley & Sons, New York, pp. 576 ISBN-10: 0471812005.
Guallini, L., Pauselli, C., Brozzetti, F., Marinangeli, L., 2015. Physical modelling of large-scale deformational systems in the South Polar Layered Deposits (Promethei Lingula, Mars): new geological constraints and climatic implications. In: In: Platz, T., Massironi, M., Byrne, P.K., Hiesinger, H. (Eds.), Volcanism and Tectonism across the Inner Solar System, vol. 401. Geological Society, London, pp. 405–421 Special Publications.
Gueydan, F., Mehl, C., Parra, T., 2005. Stress-strain rate history of a mid-crustal shear zone and the onset of brittle deformation inferred from quartz recrystallized grain size. In: In: Gapais, D., Brun, J.P., Cobbold, P.R. (Eds.), Deformation Mechanisms, Rheology and Tectonics: from Minerals to the Lithosphere, vol. 243. Geological Society, London, pp. 127–142 Special Publications.
Gudmundsson, A., 2011. Rock Fractures in Geological Processes. Cambridge University Press, Cambridge, pp. 578 ISBN: 9780511975684.
Hanmer, S., Passchier, C., 1991. Shear-sense Indicators: a Review. Geological Survey of Canada, Paper 90–17. Geological Survey of Canada, Ottawa, Canada.
Harris, R.A., Archuleta, R.J., Day, S.M., 1991. Fault steps and the dynamic rupture process: 2-D numerical simulations of a spontaneously propagating shear fracture. Geophys. Res. Lett. 18, 893–896.
Hattori, G., Trevelyan, J., Augarde, C.E., Coombs, W.M., Aplin, A.C., 2017. Numerical simulation of fracking in shale rocks: current state and future approaches. Archives Comput. Methods Eng. 24, 281–317.
Henderson, P., Henderson, G.M., 2009. The Cambridge Handbook of Earth Science Data. Cambridge University Press, Cambridge, pp. 277 ISBN: 9780521693172.
Hippertt, J.F.M., 1993. 'V'-pull-apart microstructures: a new shear-sense indicator. J. Struct. Geol. 15, 1393–1403.
Hoek, E., Martin, C.D., 2014. Fracture initiation and propagation in intact rock–a review. J. Rock Mech. Geotechnical Eng. 6, 287–300.
Hobbs, B.E., Ord, A., 2015. Structural Geology: the Mechanics of Deforming Metamorphic Rocks. Elsevier, Amsterdam, pp. 665 ISBN: 9780124078208.
Irwin, G.R., 1960. Fracture mechanics. In: 1st Symposium on Naval Structural Mechanics, pp. 557–591.
Ishii, E., 2015. Predictions of the highest potential transmissivity of fractures in fault zones from rock rheology: preliminary results. J. Geophys. Res. Solid Earth 120, 2220–2241.
Ismail-Zadeh, A., Tackley, P., 2010. Computational Methods for Geodynamics. Cambridge University Press, Cambridge, pp. 313 ISBN: 9780521867672.
Jaeger, J.C., Cook, N.G., Zimmerman, R., 2009. Fundamentals of Rock Mechanics, fourth ed. Blackwell Publishing, Malden, pp. 475 ISBN-10: 0632057599.
Jain, A.K., 1971. Stratigraphy and tectonics of lesser Himalayan region of Uttarkashi, Garhwal Himalaya. Himal. Geol. 1, 25–58.
Jefferies, S.P., Holdsworth, R.E., Wibberley, C.A.J., Shimamoto, T., Spiers, C.J., Niemeijer, A.R., Lloyd, G.E., 2006. The nature and importance of phyllonite development in crustal-scale fault cores: an example from the Median Tectonic Line, Japan. J. Struct. Geol. 28, 220–235.
Johnson, S.E., Lenferink, H.J., Price, N.A., Marsh, J.H., Koons, P.O., West, D.P., Beane, R., 2009. Clast-based kinematic vorticity gauges: the effects of slip at matrix/clast interfaces. J. Struct. Geol. 31, 1322–1339.
Kaiser, P.K., Kim, B.H., 2015. Characterization of strength of intact brittle rock considering confinement-dependent failure processes. Rock Mech. Rock Eng. 48, 107–119.
Kanagawa, K., 1993. Competence contrasts in ductile deformation as illustrated from naturally deformed chert-mudstone layers. J. Struct. Geol. 15, 865–885.
Karato, S.I., 2008. Deformation of Earth Materials: an Introduction to the Rheology of Solid Earth. Cambridge University Press, Cambridge, pp. 462 ISBN: 9780511804892.
Karato, S.I., Paterson, M.S., FitzGerald, J.D., 1986. Rheology of synthetic olivine aggregates: influence of grain size and water. J. Geophys. Res. Solid Earth 91, 8151–8176.
Kaus, B.J., 2010. Factors that control the angle of shear bands in geodynamic numerical models of brittle deformation. Tectonophysics 484, 36–47.
Keulen, N., Heolbronner, R., Stunitz, H., Boullier, A.-M., Ito, S., 2007. Grain size distributions of fault rocks: a comparison between experimentally and naturally deformed granitoids. J. Struct. Geol. 29, 1282–1300.
Kilian, R., Heilbronner, R., Stunitz, H., 2011. Quartz grain size reduction in a granitoid rock and the transition from dislocation to diffusion creep. J. Struct. Geol. 33, 1265–1284.
Kirkwood, D., Malo, M., 1993. Across-strike geometry of the Grand Pabos fault zone: evidence for Devonian dextral transpression in the Quebec Appalachians. Can. J. Earth Sci. 30, 1363–1373.
Koch, P.S., Christie, J.M., Ord, A., George Jr., , 1989. Effect of water on the rheology of experimentally deformed quartzite. J. Geophys. Res. 94, 13975–13996.
Lacroix, B., Charpentier, D., Buatier, M., Vennemann, T., Labaume, P., Adatte, T., Trave´, A., Dubois, M., 2012. Formation of chlorite during thrust fault reactivation. Record of fluid origin and P–T conditions in the Monte Perdido thrust fault (southern Pyrenees). Contributions Mineralogy Petrology 163, 1083–1102.
Lisle, R.J., 1985. Geological Strain Analysis: a Manual for the Rf/ø Method. Pergamon Press, Oxford ISBN 0-08-032590-4.
Long, S.P., Gordon, S.M., Soignard, E., 2017. Distributed north-vergent shear and flattening through Greater and Tethyan Himalayan rocks: insights from metamorphic and strain data from the Dang Chu region, central Bhutan. Lithosphere 9, 774–795.
Lu, Y., Elsworth, D., Wang, L., 2014. A dual-scale approach to model time-dependent deformation, creep and fracturing of brittle rocks. Comput. Geotechnics 60, 61–76.
Luan, F.C., Paterson, M.S., 1992. Preparation and deformation of synthetic aggregates of quartz. J. Geophys. Res. Solid Earth 97, 301–320.
Lunn, R.J., Willson, J.P., Shipton, Z.K., Moir, H., 2008. Simulating brittle fault growth from linkage of preexisting structures. J. Geophys. Res. Solid Earth 113 (B7).
Mancktelow, N.S., Pennacchioni, G., 2004. The influence of grain boundary fluids on the microstructure of quartz-feldspar mylonites. J. Struct. Geol. 26, 47–69.
Mandal, N., Samanta, S.K., Chakraborty, C., 2001. Numerical modeling of heterogeneous flow fields around rigid objects with special reference to particle paths, strain shadows and foliation drag. Tectonophysics 330, 177–194.
Mandl, G., 1999. Faulting in Brittle Rocks: an Introduction to the Mechanics of Tectonic Faults. Springer-Verlag, Berlin, Heidelberg, pp. 434 ISBN 978-3-642-08570-3.
Mandl, G., 2005. Rock Joints. Springer-Verlag, Berlin, Heidelberg ISBN-10 3-540-24553-7.
Marinho, M., Gomes, C., 2013. Structural evolution of Au, Ag and Pb lode occurrences of Serrita and Parnamirim, Pernambuco, Brazil. Braz. J. Geol. 43, 211–222.
McHenry, D., 1943. A Lattice analogy for the solution of stress problems. J. Institution Civ. Eng. 21, 59–82.
McKenzie, N.R., Hughes, N.C., Myrow, P.M., Xiao, S., Sharma, M., 2011. Correlation of Precambrian–Cambrian sedimentary successions across northern India and the utility of isotopic signatures of Himalayan lithotectonic zones. Earth Planet. Sci. Lett. 312, 471–483.
Metcalfe, R.P., 1993. Pressure, temperature and time constraints on metamorphism across the main central thrust zone and high Himalayan slab in the Garhwal Himalaya. In: In: Treloar, P.J., Searle, M.P. (Eds.), Himalayan Tectonics. Geological Society of London, vol. 74. Special Publication, pp. 485–509.
Meyer, S.E., Kaus, B., Passchier, C., 2017. Development of branching brittle and ductile shear zones: a numerical study. Geochem. Geophys. Geosystems 18, 2054–2075.
Montési, L.G., Hirth, G., 2003. Grain size evolution and the rheology of ductile shear zones: from laboratory experiments to postseismic creep. Earth Planet. Sci. Lett. 211, 97–110.
Moore, D.M., Reynolds, R.C., 1989. X-ray Diffraction and the Identification and Analysis of Clay Minerals, vol. 378. Oxford University Press, pp. 155 ISBN 019505170X.
Morales, L.F.G., Mainprice, D., Lloyd, G.E., Law, R.D., 2011. Crystal fabric development and slip systems in a quartz mylonite: an approach via transmission electron microscopy and viscoplastic self-consistent modelling. In: In: Prior, D.J., Rutter, E.H., Tatham, D.J. (Eds.), Deformation Mechanisms, Rheology and Tectonics: Microstructures, Mechanics and Anisotropy, vol. 360. Geological Society, London, pp. 151–174 Special Publications.
Mukherjee, S., 2010. V-pull apart structure in garnet in macro-scale. J. Struct. Geol. 32, 605.
Mukherjee, S., 2017. Review on symmetric structures in ductile shear zones. Int. J. Earth Sci. 106, 1453–1468.
Mukherjee, S., Carosi, R., van der Beek, P.A., Mukherjee, B.K., Robinson, D.M., 2015. Tectonics of the Himalaya: an introduction. In: In: Mukherjee, S., Carosi, R., van der Beek, P., Mukherjee, B.K., Robinson, D. (Eds.), Tectonics of the Himalaya, vol. 412. Geological Society, London, pp. 1–3 Special Publications.
Nabavi, S.T., Alavi, S.A., Mohammadi, S., Ghassemi, M.R., Frehner, M., 2017. Analysis of transpression within contractional fault steps using finite-element method. J. Struct. Geol. 96, 1–20.
Newman, W.I., 2012. Continuum Mechanics in the Earth Sciences. Cambridge University Press, Cambridge, pp. 182 ISBN: 9780511980121.
Pant, P.D., Chauhan, R., Bhakuni, S.S., 2012. Development of transverse fault along North Almora Thrust, Kumaun Lesser Himalaya, India: a study based on field and magnetic fabrics. J. Geol. Soc. India 79, 429–448.
Passchier, C.W., 1987. Stable positions of rigid objects in non-coaxial flow—a study in vorticity analysis. J. Struct. Geol. 9, 679–690.
Passchier, C.W., 1994. Mixing in flow perturbations: a model for development of mantled porphyroclasts in mylonites. J. Struct. Geol. 16, 733–736.
Passchier, C.W., Sokoutis, D., 1993. Experimental modelling of mantled porphyroclasts. J. Struct. Geol. 15, 895–909.
Passchier, C.W., Trouw, R.A.J., 2005. Microtectonics, 2nd. Springer–Verlag, Berlin, pp. 366 ISBN-10 3-540-64003-7.
Paterson, M.S., Wong, T.F., 2005. Experimental Rock Deformation-the Brittle Field. Springer, New York, pp. 347 ISBN 978-3-540-24023-5.
Peacock, D.C.P., Nixon, C.W., Rotevatn, A., Sanderson, D.J., Zuluaga, L.F., 2016. Glossary of fault and other fracture networks. J. Struct. Geol. 92, 12–29.
Peacock, D.C.P., Sanderson, D.J., Rotevatn, A., 2018. Relationships between fractures. J. Struct. Geol. 106, 41–53.
Pennacchioni, G., Fasolo, L., Cecchi, M.M., Salasnich, L., 2000. Finite-element modelling of simple shear flow in Newtonian and non-Newtonian fluids around a circular rigid particle. J. Struct. Geol. 22, 683–692.
Pepper, D.W., Heinrich, J.C., 2006. The Finite Element Method: Basic Concepts and Applications, second ed. Taylor & Francis Group, New York, pp. 312 ISBN 9781498738606.
Perez, N., 2017. Fracture Mechanics, second ed. Springer, Switzerland, pp. 418 ISBN 978-3-319-24997-1.
Pettijohn, F.J., 1984. Sedimentary Rocks, third ed. CBS Publishers and Distributors, pp. 628 ISBN 9788123908755.
Pollard, D.D., Fletcher, R.C., 2005. Fundamentals of Structural Geology. Cambridge

University Press, Cambridge, pp. 500 ISBN 0 521 83927 0.
Poppe, L.J., Paskevich, V.F., Hathaway, J.C., Blackwood, D.S., 2001. A laboratory manual for X-ray powder diffraction. U. S. Geol. Surv. Open-File Rep. 1, 1–88.
Rajendran, K., Parameswaran, R.M., Rajendran, C.P., 2017. Seismotectonic perspectives on the Himalayan arc and contiguous areas: inferences from past and recent earthquakes. Earth-Science Rev. 173, 1–30.
Ramsey, J.M., Chester, F.M., 2004. Hybrid fracture and the transition from extension fracture to shear fracture. Nature 428, 63–66.
Rashid, S.A., 2005. The geochemistry of Mesoproterozoic clastic sedimentary rocks from the Rautgara Formation, Kumaun Lesser Himalaya: implications for provenance, mineralogical control and weathering. Curr. Sci. 88, 1832–1836.
Roland, E., Behn, M.D., Hirth, G., 2010. Thermal-mechanical behavior of oceanic transform faults: implications for the spatial distribution of seismicity. Geochem. Geophys. Geosystems 11, Q07001.
Rutter, E.H., Brodie, K.H., 2004. Experimental intracrystalline plastic flow in hot-pressed synthetic quartzite prepared from Brazilian quartz crystals. J. Struct. Geol. 26, 259–270.
Sandiford, M., Hansen, D.L., McLaren, S.N., 2006. Lower crustal rheological expression in inverted basins. In: In: Buiter, S.J.H., Schreurs, G. (Eds.), Analogue and Numerical Modelling of Crustal-scale Processes, vol. 253. Geological Society, London, pp. 271–283 Special Publications.
Sengupta, S., Chatterjee, S.M., 2015. Microstructural variations in quartzofeldspathic mylonites and the problem of vorticity analysis using rotating porphyroclasts in the Phulad Shear Zone, Rajasthan, India. In: Mukherjee, S., Mulchrone, K.F. (Eds.), Ductile Shear Zones: from Micro-to Macro-scales. Wiley Blackwell, pp. 128–140.
Skempton, A.W., 1966. Some observations on tectonic shear zones. In: 1st ISRM Congress. International Society for Rock Mechanics, pp. 1–7.
Stipp, M., StuÈnitz, H., Heilbronner, R., Schmid, S.M., 2002. The eastern Tonale fault zone: a ‘natural laboratory’ for crystal plastic deformation of quartz over a temperature range from 250 to 700 C. J. Struct. Geol. 24, 1861–1884.
Stoeckhert, F., Molenda, M., Brenne, S., Alber, M., 2015. Fracture propagation in sandstone and slate–Laboratory experiments, acoustic emissions and fracture mechanics. J. Rock Mech. Geotechnical Eng. 7, 237–249.
Tadmor, E.B., Miller, R.E., Elliott, R.S., 2012. Continuum Mechanics and Thermodynamics: from Fundamental Concepts to Governing Equations. Cambridge University Press, Cambridge, pp. 350 ISBN: 9781139017657.
Takahashi, T., Tanaka, S., 2017. Compressive strength–seismic velocity relationship for sedimentary rocks. In: Ting-Feng, X. (Ed.), Rock Mechanics and Engineering Volume 1: Principles. Taylor & Francis Group, London, pp. 299–322.
Tang, C.A., Liu, H., Lee, P.K.K., Tsui, Y., Tham, L.G., 2000. Numerical studies of the influence of microstructure on rock failure in uniaxial compression—part I: effect of heterogeneity. Int. J. Rock Mech. Min. Sci. 37, 555–569.
TerHeege, J.H., deBresser, J.H.P., Spiers, C.J., 2002. The influence on dynamic recrystallization on the grain size distribution and rheological behaviour of Carrara marble deformed in axial compression. In: In: de Meer, S., Drury, M.R., de Bresser, J.J.P., Pennock, G.M. (Eds.), Deformation Mechanisms, Rheology and Tectonics: Current Status and Future Perspectives, vol. 200. Geological Society, London, pp. 331–353 Special Publications.
Tetreault, J.Á., Buiter, S.J.H., 2012. Geodynamic models of terrane accretion: testing the fate of island arcs, oceanic plateaus, and continental fragments in subduction zones. J. Geophys. Res. Solid Earth 117, B08403.
Thakur, V.C., 1992. Geology of Western Himalaya. Pergamon Press, Oxford.
Thakur, V.C., Kumar, S., 1994. Seismotectonics of the 20 October 1991 Uttarkashi Earthquake in Garhwal, vol. 6. Terra Nova, Himalaya, North India, pp. 90–94.
Thompson, G.A., Parsons, T., 2016. Vertical deformation associated with normal fault systems evolved over coseismic, postseismic, and multiseismic periods. J. Geophys. Res. Solid Earth 121, 2153–2173.
Treagus, S.H., 1988. Strain refraction in layered systems. J. Struct. Geol. 10, 517–527.
Turcotte, D., Schubert, G., 2014. Geodynamics, third ed. Cambridge University Press, Cambridge ISBN: 9780521186230, 636 pp.
Twiss, R.J., Moores, E.M., 2007. Structural Geology, second ed. Macmillan, pp. 736 ISBN-10: 0-7167-4951-3.
Valdiya, K.S., 1980. Geology of Kumaun lesser Himalaya. Wadia Institute of Himalayan geology. Dehradun 291.
Valdiya, K.S., 2010. The Making of India: Geodynamic Evolution, second ed. Springer, pp. 303–350 ISBN 978-3-319-25029-8.
Warren, J.M., Hirth, G., 2006. Grain size sensitive deformation mechanisms in naturally deformed peridotites. Earth Planet. Sci. Lett. 248, 438–450.
Wei, C.H., Zhu, W.C., Yu, Q.L., Xu, T., Jeon, S., 2015. Numerical simulation of excavation damaged zone under coupled thermal–mechanical conditions with varying mechanical parameters. Int. J. Rock Mech. Min. Sci. 75, 169–181.
Wenk, H.R., Pannetier, J., 1990. Texture development in deformed granodiorites from the Santa Rosa mylonite zone, southern California. J. Struct. Geol. 12, 177–184.
Wilson, J.P., Lunn, R.J., Shipton, Z.K., 2007. Simulating spatial and temporal evolution of multiple wing cracks around faults in crystalline basement rocks. J. Geophys. Res. Solid Earth 112, B08408.
Wu, Z., Fan, L., Liu, Q., Ma, G., 2017. Micro-mechanical modeling of the macro-mechanical response and fracture behavior of rock using the numerical manifold method. Eng. Geol. 229, 49–60.
Xia, H., Platt, J.P., 2018. Quartz grainsize evolution during dynamic recrystallization across a natural shear zone boundary. J. Struct. Geol. 109, 120–126.
Xu, T., Tang, C.A., Zhao, J., Li, L., Heap, M.J., 2012. Modelling the time-dependent rheological behaviour of heterogeneous brittle rocks. Geophys. J. Int. 189, 1781–1796.
Xypolias, P., 2010. Vorticity analysis in shear zones: a review of methods and applications. J. Struct. Geol. 32, 2072–2092.
Xypolias, P., Koukouvelas, I.K., 2001. Kinematic vorticity and strain rate patterns associated with ductile extrusion in the Chelmos Shear Zone (External Hellenides, Greece). Tectonophysics 338, 59–77.
Zhang, Q.B., Zhao, J., 2014. Quasi-static and dynamic fracture behaviour of rock materials: phenomena and mechanisms. Int. J. Fract. 189, 1–32.
Zhang, Y.J., 2016. Geometric Modeling and Mesh Generation from Scanned Images, vol. 6. Taylor & Francis Group, Boca Raton, pp. 340 ISBN 9781482227765.
Zhang, P., Li, X.B., Li, N., 2008. Strength evolution law of cracked rock based on localized progressive damage model. J. Central South Univ. Technol. 15, 493–497.
Zhu, W.C., Tang, C.A., 2002. Numerical simulation on shear fracture process of concrete using mesoscopic mechanical model. Constr. Build. Mater. 16, 453–463.
Zienkiewicz, O.C., Taylor, R.L., 2000. fifth ed. The Finite Element Method: Basic Formulation and Linear Problems, vol. I. McGraw-Hill, New York, pp. 589 ISBN 0 7506 5049 4.